J. Fluid Mech. (1975), *vol.* 70, *part* 4, *pp.* 705–720
Printed in Great Britain

Pressure- and buoyancy-driven thermal convection in a rectangular enclosure

By L. W. SPRADLEY
Lockheed Missiles and Space Company, Huntsville, Alabama 35807

AND S. W. CHURCHILL
Department of Chemical and Biochemical Engineering,
University of Pennsylvania, Philadelphia 19174

(Received 1 April 1974 and in revised form 20 February 1975)

Results are presented for unsteady laminar thermal convection in compressible fluids at various reduced levels of gravity in a rectangular enclosure which is heated on one side and cooled on the opposite side. The results were obtained by solving numerically the equations of conservation for a viscous, compressible, heat-conducting, ideal gas in the presence of a gravitational body force. The formulation differs from the Boussinesq simplification in that the effects of variable density are completely retained. A conservative, explicit, time-dependent, finite-difference technique was used and good agreement was found for the limited cases where direct comparison with previous investigations was possible. The solutions show that the thermally induced motion is acoustic in nature at low levels of gravity and that the unsteady-state rate of heat transfer is thereby greatly enhanced relative to pure conduction. The nonlinear variable density profile skews the streamlines towards the cooler walls but is shown to have little effect on the steady-state isotherms.

1. Introduction

In recent years finite-difference computation on a digital computer has been used successfully as a means of analysing and gaining insight into complex problems in many aspects of fluid mechanics. Our knowledge of natural convection flows in particular has increased immensely because the nonlinear effects and coupled phenomena in this type of flow can now be analysed. Most analytical treatments of natural convection invoke the Boussinesq approximation, which neglects the effects of fluid compressibility other than in the generation of buoyancy forces. In the weak gravitational field of space, convection due to buoyancy is virtually eliminated (Grodzka & Bannister 1972). The need then arises to assess the role of convective driving mechanisms other than gravity. The convection considered here in addition to that due to buoyancy is the pressure-driven convection which results when a confined compressible fluid is heated rapidly. This type of motion has been termed thermo-acoustic convection owing to the sonic character of the induced pressure waves. The objective of the present

investigation is to analyse thermal convection of a compressible fluid including the unsteady effects of pressure- and buoyancy-driven fluid motion.

The literature on analysis of buoyancy-driven natural convection by numerical methods is too extensive to review here. Specific reference, however, will be made later to the work of Hellums & Churchill (1962), Wilkes & Churchill (1966), Torrance (1968) and Torrance *et al.* (1972). Analytical studies of pressure-driven convection have received considerably less attention. Harlow & Amsden (1971) made calculations for fluids of variable density but not for thermally induced wave motion. Trilling (1955), Knudsen (1957) and Luikov & Berkovsky (1970) were among the first to investigate analytically the wave motion induced in gases by boundary-temperature gradients. These investigators used a linear perturbation analysis and found that a sharp rise in boundary temperature can cause pressure waves to propagate through the fluid in much the same manner as pushing a piston through a gas-filled pipe. Larkin (1967) was apparently the first to use finite-difference methods to solve the equations of conservation for conditions leading to thermally induced acoustic waves. He considered one-dimensional motion of an ideal gas in a confined region at zero gravity. His computations confirm the acoustic nature of the wave motion and indicate that the heat transfer and pressure rise are greatly enhanced over those in an analytical solution which neglects thermally induced fluid motion. Thuraisamy (1972) applied Larkin's numerical method to analyse the flow of supercritical oxygen in spacecraft tanks. He used a one-dimensional model with zero gravity and successfully simulated the thermally induced wave motion. Heinmiller (1970) used finite-difference methods to analyse the convective flow in spacecraft fuel tanks at low gravity. His two-dimensional model, which includes a buoyancy force, variable density and real-fluid properties, was used to simulate pressure collapse phenomena in oxygen storage systems. Spradley *et al.* (1973) used a finite-difference method to compute thermo-acoustic convection in a confined ideal gas at zero gravity. The results of their analysis indicate that pressure and thermal expansion effects can be significant factors in determining the motion and rate of heat transfer through confined fluids which are heated rapidly. A numerical algorithm using finite differences was developed for solving the differential equations for the conservation of mass, momentum and energy in compressible flow. A modified form of this algorithm was used in the present investigation to compute the two-dimensional flow of an ideal gas in a rectangular enclosure including both buoyancy and pressure effects.

This paper is divided as follows. The mathematical formulation of the governing equations, including the initial and boundary conditions and a dimensional analysis, is given in § 2. A description of the finite-difference technique, the computation algorithm and the stability and conservational features constitutes §3. A discussion of illustrative calculations which have been carried out is presented in § 4.

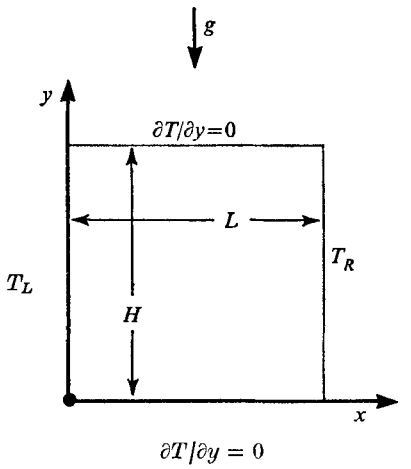

FIGURE 1. Geometric configuration and co-ordinate system.

2. Mathematical formulation

Consider a 'two-dimensional' rectangular enclosure of length L and height H which contains compressible fluid as shown in figure 1. The fluid is initially motionless with a uniform temperature T_0. The upper and lower walls are perfectly insulated and the side walls are maintained at temperatures T_L and T_R. The Eulerian formulation is adopted and a Cartesian co-ordinate system is used with the gravitational vector in the direction of the $-y$ axis. Laminar flow and an ideal gas which is compressible, viscous and heat conducting are assumed. The thermal conductivity k, viscosity μ and specific heat C_v are assumed to be constant, but variations in density are taken into account. Kinetic energy, radiative transfer, internal heat sources and viscous dissipation of energy are neglected. Justification for the neglect of kinetic energy and viscous dissipation is provided at the end of this section. The pressure is related to the density and temperature through the ideal-gas law.

The independent variables are the spatial co-ordinates x and y and the time t. The problem can be described in terms of the following dependent variables: the velocity components (u, v) in the (x, y) directions, the density ρ, temperature T and pressure P. The governing equations are those for the conservation of momentum, mass and energy in the region, plus the ideal-gas law. These equations, which are written in conservation-law or divergence form, are given below in terms of dimensionless variables.

x momentum

$$\frac{\partial}{\partial t}(\rho u)+\frac{\partial}{\partial x}(\rho uu)+\frac{\partial}{\partial y}(\rho uv) = -\frac{\partial P}{\partial x}+\frac{1}{Re}\left(\frac{4}{3}\frac{\partial^2 u}{\partial x^2}+\frac{1}{3}\frac{\partial^2 v}{\partial x\,\partial y}+\eta^2\frac{\partial^2 u}{\partial y^2}\right). \tag{1}$$

y momentum

$$\frac{\partial}{\partial t}(\rho v)+\frac{\partial}{\partial x}(\rho vu)+\frac{\partial}{\partial y}(\rho vv) = -\eta^2\left(\frac{1}{Fr}\rho+\frac{\partial P}{\partial y}\right)+\frac{1}{Re}\left(\frac{4}{3}\eta^2\frac{\partial^2 v}{\partial y^2}+\frac{1}{3}\eta^2\frac{\partial^2 u}{\partial x\,\partial y}+\frac{\partial^2 v}{\partial x^2}\right). \tag{2}$$

Continuity

$$\frac{\partial \rho}{\partial t} + \frac{\partial}{\partial x}(\rho u) + \frac{\partial}{\partial y}(\rho v) = 0. \tag{3}$$

Energy

$$\frac{\partial}{\partial t}(\rho T) + \frac{\partial}{\partial x}(\rho u T) + \frac{\partial}{\partial y}(\rho v T) = (1-\gamma)\left[\frac{\partial}{\partial x}(Pu) + \frac{\partial}{\partial y}(Pv)\right] + \frac{\gamma}{Re\,Pr}\left(\frac{\partial^2 T}{\partial x^2} + \eta^2 \frac{\partial^2 T}{\partial y^2}\right). \tag{4}$$

State

$$P = \rho T. \tag{5}$$

The initial and boundary conditions are expressed in dimensionless form as follows.

Initial conditions

$$\left.\begin{aligned} u(x,y,0) = v(x,y,0) = 0, \quad T(x,y,0) = 1, \\ \partial P(x,y,0)/\partial y = -Fr^{-1}\rho(x,y,0), \quad \rho(x,y,0) = P(x,y,0). \end{aligned}\right\} \tag{6}$$

Boundary conditions

$$\left.\begin{aligned} u = v = 0 \quad \text{at all walls}, \\ T(0,y,t) = T_L, \quad T(1,y,t) = T_R, \\ \partial T(x,0,t)/\partial y = \partial T(x,1,t)/\partial y = 0. \end{aligned}\right\} \tag{7}$$

The dimensionless variables are

$$\left.\begin{aligned} x = x'/L, \quad y = y'/H, \quad t = t'(\mathscr{R}T'_0/M)^{\frac{1}{2}} L^{-1}, \\ u = u'(\mathscr{R}T'_0/M)^{-\frac{1}{2}}, \quad v = v'(L/H)(\mathscr{R}T'_0/M)^{-\frac{1}{2}}, \quad g = g'/g'_{\text{earth}}, \\ \rho = \rho'/\rho'_0, \quad T = T'/T'_0, \quad P = P'M/(\rho'_0 \mathscr{R}T'_0), \end{aligned}\right\} \tag{8}$$

where primes designate the original dimensional variables, $\mathscr{R}$ is the universal gas constant and M is the molecular weight of the gas.

The dimensionless parameters in the governing equations are

$$\left.\begin{aligned} \eta &= L/H \quad \text{(aspect ratio)}, \\ \gamma &= C'_p/C'_v \quad \text{(ratio of specific heats)}, \\ Pr &= \gamma C'_v \mu'/k' \quad \text{(Prandtl number)}, \\ Re &= \rho'_0 L(\mathscr{R}T'_0/M)^{\frac{1}{2}}(\mu')^{-1} \quad \text{(acoustic Reynolds number)}, \\ Fr &= \mathscr{R}T'_0/Hg'M \quad \text{(acoustic Froude number)}. \end{aligned}\right\} \tag{9}$$

Additional dimensionless groups referred to later in the analysis are

$$\begin{aligned} Re_f &= \rho' L V'/\mu' \quad \text{(flow Reynolds number)}, \\ Gr &= \rho'^2_0 g' \beta' (T'_L - T'_R) L^3/\mu'^2 \quad \text{(Grashof number)}, \\ Nu &= h' L/k' \quad \text{(Nusselt number)}. \end{aligned}$$

The additional symbols used above are V', the maximum flow velocity, β', the volume coefficient of thermal expansion and h', the local heat-transfer coefficient.

The classic approach to computation of natural convection is to invoke the Boussinesq approximation, introduce a stream function and write the governing

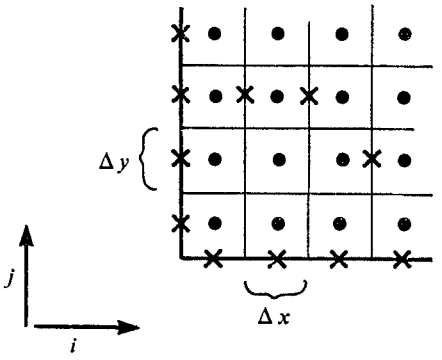

FIGURE 2. Cell-centred finite-difference grid. ●, cell centre; ×, cell boundary.

equations in vorticity–stream-function form. This approach is not taken in the present analysis but rather solutions are obtained for the primitive variables [(1)–(5)]. The initial formulation included both the kinetic energy and viscous dissipation terms in the energy equation. A numerical study was made of typical cases which included these effects or in which they were neglected one at a time. This study showed clearly that, for the conditions considered here, both effects are negligible. (Results of a portion of the study of the effect of viscous dissipation are given by Spradley *et al.* (1973).) Hence these terms were removed from the formulation to produce a more efficient computer code. The computations carried out included sufficient points within the boundary layer to justify the use of no-slip boundary conditions.

3. Numerical method

The numerical method employed in this analysis is based on explicit finite-difference approximations. The use of the unsteady equations allows a forward-time-marching algorithm to be used since the problem is of initial-value type. Values of the dependent variables are specified at time $t = 0$ at a finite number of discrete points on a numerical grid. The differential equations are approximated at these grid points by difference equations. The algorithm used here is based on a combination of techniques presented in the literature plus some innovations. A review of finite-difference approximations for natural convection is given by Torrance (1968). However, these techniques have been applied only to the quasi-incompressible equations resulting from the Boussinesq approximation. The finite-difference approximations used in the present study are patterned on method V of Torrance (1968) with appropriate modification for compressibility. The technique is conditionally stable, free of a spatial mesh restriction and numerically conservative.

The explicit approach chosen here requires smaller time steps to ensure numerical stability than an implicit formulation. However, an implicit method would require time steps of the same size in order to simulate the acoustic wave motion. Since it is the physical phenomena of acoustic waves that limits the time

step, rather than stability, an explicit approach is here more efficient than an implicit scheme.

A cell-centred finite-difference grid (shown in figure 2) is used to write down the difference equations. All flow variables are evaluated at the centre of a cell and differences are taken across a cell using the known values in adjacent cells and/or interpolated values at the boundaries of the cells. The boundary conditions, however, are specified at the walls themselves and not at the centre of the cell adjacent to the wall. In the difference equations, the subscripts i and j refer to spatial locations in the x and y directions respectively, and the superscript n denotes time, i.e. $t = n\Delta t$. The grid points are thus defined as $x_i = (i-\frac{1}{2})\Delta x$, $y_j = (j-\frac{1}{2})\Delta y$. The grid spacings Δx and Δy are constant but not necessarily equal.

Forward time differences are used to approximate the unsteady derivatives:

$$[\partial f/\partial t]_{ij}^{n+1} \approx (f_{ij}^{n+1} - f_{ij}^{n})/\Delta t, \tag{10}$$

where f represents any of the variables ρu, ρv, ρ and T. This approach yields a finite-difference approximation which is of first order in time.

The particular form of the space-difference operator depends on the type of term to which it is applied. There are basically four types of terms in the governing equations: first-order terms, second-order terms, cross-terms and convection terms. Many schemes were considered and tested. Table 1 summarizes the types of terms and shows the finite-difference approximations which were chosen. Centred differences were used except for the convection terms. A donor difference scheme is necessary for the convection terms in order to preserve numerical stability in the explicit approach as discussed by Hellums & Churchill (1962). The conservative donor method, which is patterned on Torrance's method V, was applied to all the convection terms in the momentum and energy equations.

The donor operator is known to introduce a numerical diffusion effect owing to the first-order spatial truncation error. For certain types of flow, especially at high Reynolds number, the magnitude of the numerical diffusion can be larger than the real diffusion. As pointed out by many investigators, including Torrance *et al.* (1972) and Harlow & Amsden (1971), these fictitious effects can be reduced by refining the grid network or by using some other form of differencing such as the ZIP technique. The technique used here, commonly called the donor cell method, is preferred owing to the severity of the thermal boundary conditions, i.e. very rapid heating. The contributions of the numerical diffusion effects were tested by using refined grid spacings and found not to influence the solutions significantly. Particular note should be made of the convective difference operators in table 1. The function f is transported from cell to cell using the average velocity between the cells. It is this type of operator that leads to a high degree of conservation. Central differences could be used in the continuity equation because the ρu and ρv terms that appear are evaluated at time $n+1$. This equation is effectively implicit but could be evaluated explicitly since $(\rho u)^{n+1}$ and $(\rho v)^{n+1}$ were known and ρ^{n+1} was to be determined. This technique is conditionally stable and conserves mass identically on a numerical grid.

The difference operators for a cell adjacent to a wall must have a special form.

Type of term	Differential form	Finite-difference approximation
First order	$\partial f/\partial x$	$(f^n_{i+1,j}-f^n_{i-1,j})/(2\Delta x)$
Second order	$\partial^2 f/\partial x^2$	$(f^n_{i+1,j}-2f^n_{i,j}+f^n_{i-1,j})/(\Delta x)^2$
Cross	$\partial^2 f/\partial x\,\partial y$	$(f^n_{i+1,j+1}+f^n_{i-1,j-1}-f^n_{i+1,j-1}-f^n_{i-1,j+1})/4\Delta x\Delta y$
Convection	$\partial(uf)/\partial x$	$\begin{cases}(u^n_{i+\frac{1}{2},j}f^n_{i+1,j}-u^n_{i-\frac{1}{2},j}f^n_{ij})/\Delta x & \text{if } u^n_{i+\frac{1}{2},j},\, u^n_{i-\frac{1}{2},j}\leqslant 0\\ (u^n_{i+\frac{1}{2},j}f^n_{i,j}-u^n_{i-\frac{1}{2},j}f^n_{i-1,j})/\Delta x & \text{if } u^n_{i+\frac{1}{2},j},\, u^n_{i-\frac{1}{2},j}>0\\ (u^n_{i+\frac{1}{2},j}\bar{f}^n_{i+1,j}-u^n_{i-\frac{1}{2},j}\bar{f}^n_{i-1,j})/\Delta x & \text{if } u^n_{i+\frac{1}{2},j},\, u^n_{i-\frac{1}{2},j} \text{ of opposite sign}\end{cases}$

Notes

$$\bar{f}^n_{i\pm1,j}=\begin{cases}f^n_{i\pm1,j} & \text{if } u^n_{i+\frac{1}{2},j}<0,\quad u^n_{i-\frac{1}{2},j}>0\\ f^n_{i,j} & \text{if } u^n_{i+\frac{1}{2},j}>0,\quad u^n_{i-\frac{1}{2},j}<0\end{cases}$$

$$u^n_{i\pm\frac{1}{2},j}=\tfrac{1}{2}(u^n_{i,j}+u^n_{i\pm1,j})$$

TABLE 1. Finite-difference approximations

The technique employed here consists of obtaining a value at a cell boundary by averaging over two adjacent cells and then differencing across the cell. For example

$$\partial f^n_{1j}/\partial x=[\tfrac{1}{2}(f^n_{1j}+f^n_{2j})-f^n_{wj}]/\Delta x \tag{11}$$

is used to compute $\partial f/\partial x$ for the $i=1$ cells. This form assumes that f^n_{wj} is prescribed along $x=0$. This form is thus used for the ρu and ρv differences for all cells adjacent to walls and for the T differences for cells adjacent to the left and right walls. The T differences for cells adjacent to the upper and lower walls are obtained by calculating a cell boundary gradient $(T^n_{i,2}-T^n_{i,1})/\Delta y$ and then averaging with the known zero gradient at the adiabatic wall. The pressure differences for a cell adjacent to a wall are obtained by using quadratic extrapolation to obtain the pressure at the wall and then using central differences to calculate gradients.

This explicit finite-difference method for solution of the compressible flow equations is a conditionally stable technique. A restriction is imposed on the size of the time step Δt to ensure numerical stability. The criterion for Δt was found by numerical experimentation since a rigorous stability analysis for such complex equations is beyond the state of the art. The most restrictive time step was found to be given by the hyperbolic limit (Richtmyer & Morton 1967, p. 323), which expressed in the dimensionless variables is

$$\Delta t<\Delta/(2\gamma T_h)^{\frac{1}{2}}, \tag{12}$$

where Δ is the smallest grid spacing in the network and T_h is the largest temperature. This value represents essentially the time required for a wave to move a distance of one cell width. In real time this corresponds to time steps of the order of 10^{-3}s. For problems requiring several seconds of simulation, this is not severely restrictive for current computer systems. A time-scaling procedure is used to reduce the computer run time for problems requiring long simulation times such as obtaining steady-state solutions. The time-scaling method, which

is based on similarity principles, was originally proposed by Heinmiller (1970) and details of its application to this problem are given by Spradley *et al.* (1973).

The algorithm used for the computations can be summarized as follows.

(i) Given conditions at each grid point at time n, the products ρu and ρv are advanced to time $n+1$ using (1) and (2), respectively.

(ii) The products ρu and ρv at time $n+1$ are used in (3) to obtain the density ρ at time $n+1$.

(iii) The temperature T at $n+1$ is now calculated from (4) using the value just computed for ρ^{n+1}.

(iv) The pressure P at time $n+1$ is evaluated explicitly using (5), and the velocity components u and v are obtained from the ρu, ρv and ρ calculations.

(v) The process is repeated until $t = t_{\max}$ or until a steady state is reached.

A computer program using FORTRAN V was developed to implement this numerical algorithm on the Univac 1108 multiprocessor system.

4. Discussion of results

Results of illustrative calculations are presented here and others may be found in reports by Spradley *et al.* (1973) and Bannister *et al.* (1973). The objective of the sample calculations presented here is (i) to verify the numerical method by comparison with previous solutions, (ii) to illustrate the general effects of a variable density profile, (iii) to show the unsteady effects of pressure convection on the isotherms, and (iv) to present a complete steady-state map of the flow field for a representative case. The first case consists of a one-dimensional simulation of a zero-gravity problem for comparison with the solutions of Larkin (1967) and Thuraisamy (1972). The second case consists of buoyancy-driven natural convection for comparison with the results of Wilkes & Churchill (1966). The third case is for unsteady convection in a container of helium gas at varying levels of gravity.

Convergence of the numerical solutions was established for all cases by comparing results for different grid spacings. Extrapolation of the results for selected cases for 10×10, 20×20 and 30×30 grids to zero grid spacing confirmed convergence of the numerical scheme. The steady-state results for the 10×10 grid differed by less than 4 % from the extrapolated values for the Nusselt number and by less than 6 % for the temperature, density and velocity at the centre of the grid. The results for the 20×20 grid differed by less than 1 % from the extrapolated values and the results for the 30×30 grid differed negligibly. In the interest of computational economy the calculations were generally carried out only for a 10×10 grid and the results presented here are for such a grid unless specified otherwise. The use of a conservative finite-difference scheme is believed to be responsible for the reasonable accuracy of the solutions for such a coarse grid as discussed by Torrance *et al.* (1972). The dependence of the solutions on Δt was also checked by using different step sizes until significant changes in the unsteady profiles were no longer apparent. Dimensionless values of the order of 0·01 were found to be the best compromise of accuracy and machine time. Test calculations were also carried out for the initial period using a scheme of Dufort–

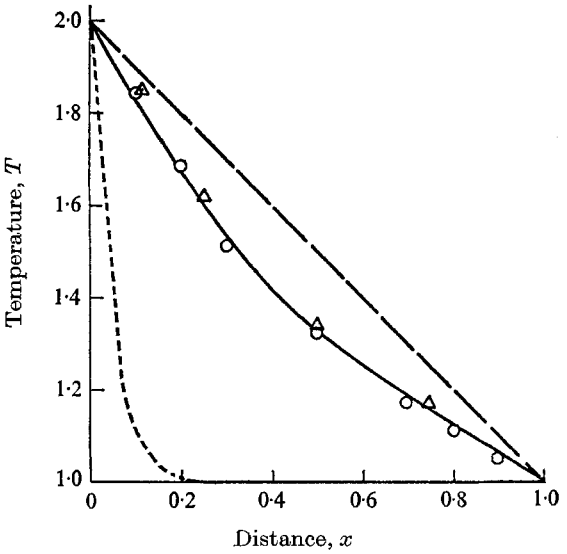

FIGURE 3. Temperature *vs.* x at $y = 0{\cdot}5$ for $t = 1000$. – – –, conduction; ——, convection; ——, steady state; ○, Larkin; △, Thuraisamy.

Frankel type. The results are in excellent agreement. The steady-state solutions presented here required an average of 10 min of computer processing units on the Univac 1108 system.

The first example was chosen to verify the technique for a zero-gravity problem and to investigate the effects of pressure convection in the absence of buoyancy. This problem has been solved by Larkin (1967) and Thuraisamy (1972) and is described in detail by Spradley (1973). The problem consists of one-dimensional flow of helium gas between parallel plates. The fluid motion is driven entirely by pressure gradients induced by the thermal boundary conditions. The one-dimensional situation is simulated here by using a large aspect ratio $\eta = 100$ and by setting $g = 0$ and $v = 0$. The thermal boundary conditions consist of $T_L = 2$ and $T_R = 1$ with the dimensionless groups $Re = 1{\cdot}2 \times 10^6$, $Pr = 0{\cdot}685$ and $\gamma = 1{\cdot}67$. The solution was marched forward in time until the one-dimensional motion was highly damped and the temperature closely approached the steady-state form $T = 2 - x$. The profile of T *vs.* x at $t = 1000$ is compared in figure 3 with the results of Larkin and Thuraisamy. Excellent agreement is apparent. This figure also illustrates that pressure-driven convection is an effective mechanism of heat transfer. The solution has almost reached a steady state at $t = 1000$ while for pure conduction the heat has penetrated into only 20 % of the region. The pressure profile was found to converge to the constant steady-state value of 1·44 as the velocity waves damped out. This one-dimensional simulation shows that the solution scheme can adequately calculate the flow profiles in the absence of buoyancy.

The second example consists of the calculation of the steady-state profiles for buoyancy-driven flow in a rectangular region as considered by Wilkes & Churchill (1966). Their configuration and the boundary conditions are identical to those in

FIGURE 4. Steady-state temperature and stream-function maps for comparison with solution of Wilkes & Churchill. (10 = max, 1 = min.) (*a*) Contours of T: min = 0·518, max = 1·47. (*b*) Contours of ψ: min = $2{\cdot}0 \times 10^{-8}$, max = $1{\cdot}02 \times 10^{-5}$.

the present formulation. An exact simulation is not possible since the present solution includes pressure effects and a variable density profile. Qualitative comparison is possible, however, and should serve to verify the procedure. The thermal boundary conditions are $T_L = 0{\cdot}5$ and $T_R = 1{\cdot}5$. The dimensionless parameters (Re, Fr, etc.) were chosen to produce a Grashof number $Gr = 2{\cdot}0 \times 10^4$, Prandtl number $Pr = 0{\cdot}733$ and an aspect ratio $\eta = 1{\cdot}0$, which simulates the problem of Wilkes & Churchill. The solution was marched forward in time until a steady state was attained. In this procedure the velocity profiles are combined according to the classic definition to produce the stream function ψ:

$$\partial\psi/\partial x = -\rho v, \quad \partial\psi/\partial y = \rho u. \tag{13}$$

A sub-program then maps the flow contours using the line printer. The minimum and maximum values of the stream function are mapped as 1 and 10 respectively with intermediate values at equal increments mapped onto 2–9 (even numbers are mapped with blanks for clarity). The contour maps correspond to the cell-centred grid in figure 2. No extrapolation is made to the walls, thus the maps do not show a minimum $\psi = 0$ since the wall conditions are not mapped. The boundary condition $\psi = 0$ is used, however, to solve for the stream function from the calculated velocity profiles. The tick marks on the contour maps correspond to the centre of a cell where all calculations were made.

Figure 4 gives the steady-state maps of the temperature and stream function for the problem of Wilkes & Churchill. The isotherms agree in both shape and magnitude with the calculations presented in their figure 5. (The isotherm $T = 1$ in the present solution corresponds to $T = 0$ in theirs.) The stream-function maps have the same basic shape as those in their figure 6 but are skewed somewhat towards the cooler regions of the fluid, i.e. to the left and bottom of the container. This is a direct result of the variable density, which produces a different buoyancy in the cold and hot regions giving the asymmetry shown. The magnitudes of the

FIGURE 5. Steady-state temperature and stream-function maps illustrating variable-density effects. (10 = max, 1 = min.) (*a*) Contours of T: min = 0·528, max = 1·46. (*b*) Contours of ψ: min = $1{\cdot}68 \times 10^{-10}$, max = $4{\cdot}07 \times 10^{-7}$.

stream functions shown in figure 4 are considerably different owing to the different reference velocity used here, but when these values are converted to the form used by Wilkes & Churchill, the agreement in magnitude is excellent. The present calculations give values of ψ which are on average 40 % larger in some regions and 25 % smaller in other regions. This apparent discrepancy is understandable, however, since the definition of the stream function used in (13) is for variable-density flow and the density variations range from 1·4 to 0·7.

Further verification is evident from the steady-state Nusselt number. The average Nusselt number $\overline{Nu}$ is obtained by integrating $\partial T/\partial x$ along the walls $x = 0$ and $x = 1$. Wilkes & Churchill give $\overline{Nu} = 2{\cdot}87$ for a 10×10 grid and $\overline{Nu} = 2{\cdot}52$ for a 20×20 grid. Steady-state values of 2·69 and 2·63 were obtained with the present analysis using 10×10 and 20×20 grids, respectively. This close agreement suggests that the density variations do not appreciably affect the steady-state Nusselt number. The isotherms were also affected very little by the variable density.

Further investigation was made of the effects of variable density on the orientation of streamlines and isotherms. The Wilkes & Churchill configuration was used but with a gravity level $g = 0{\cdot}1$, which reduces Gr to $2{\cdot}0 \times 10^3$. The same boundary conditions and dimensionless groups were used except for the Froude number, which is now based on $g = 0{\cdot}1$. Figure 5 shows the steady-state maps for this case. The temperature retains an almost symmetric character, but the stream function is even more asymmetric than in the case $g = 1{\cdot}0$ (figure 4). The thermal boundary conditions should produce nearly symmetric streamlines under the Boussinesq approximation, but the variable density employed here results in buoyancy of different magnitude in the cold and hot regions of the fluid since ρ does not depend on ΔT alone. This effect appears to be more pronounced for lower gravity levels, i.e., larger Froude numbers, as may be seen by comparing figures 4 and 5.

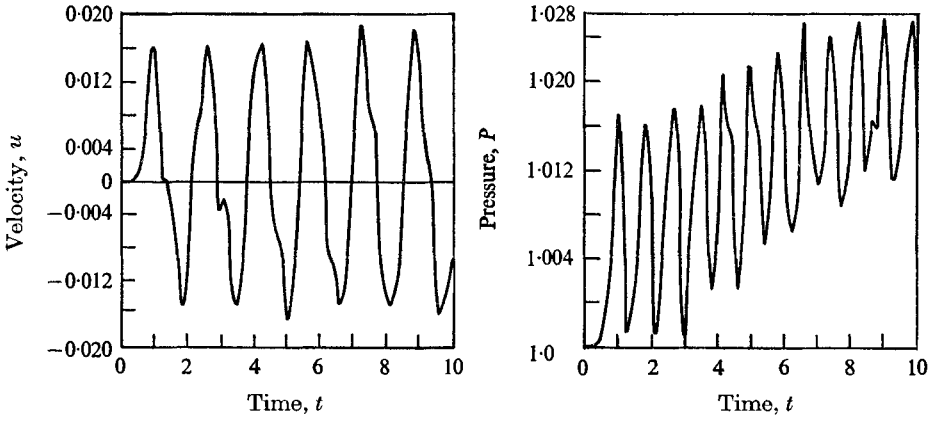

FIGURE 6. Velocity and pressure *vs.* time at initiation of motion. ($x = 0{\cdot}5$, $y = 0{\cdot}45$.)

The third case considers the flow of helium gas in a rectangular container to illustrate the combined effects of buoyancy- and pressure-driven convection. The fluid is assumed to be initially motionless with initial conditions $T_0' = 273\,^{\circ}\mathrm{K}$ and $P_0' = 1{\cdot}08 \times 10^6$ dyne/cm^2. The thermal boundary conditions are $T_L = 2{\cdot}0$ and $T_R = 1{\cdot}0$, with the following governing parameters:

$$\eta = 1{\cdot}0, \quad Re = 2{\cdot}07 \times 10^5, \quad Pr = 0{\cdot}685, \quad \gamma = 1{\cdot}67,$$

$$Fr = 2{\cdot}15 \times 10^6 \quad \text{(based on } g = 1{\cdot}0\text{)}.$$

The Froude number is varied to investigate the effects of different gravity levels.

The motion is initiated at the left wall ($x = 0$) as the fluid expands upon being heated. The thermally induced waves propagate in the $+x$ direction and are subsequently reflected from the wall $x = 1$. The motion at early times is driven by the $\partial P/\partial x$ term in the x-momentum equation and is one-dimensional. Figure 6 shows the x component of velocity and the pressure *vs.* time at the location $x = 0{\cdot}5$, $y = 0{\cdot}45$ in the container. The waves have the local acoustic period $2/(\gamma T)^{\frac{1}{2}}$. The velocity amplitudes are approximately 0·02 of sonic at the initiation of motion but are damped rapidly with time. The pressure waves are seen to follow the velocity with twice the effective frequency. This is due to the effects on pressure of both left- and right-running velocity waves. This early motion is one-dimensional and is identical to the solution reported by Spradley (1973).

Figure 6 indicates that at short times Mach numbers of the order of 10^{-2} are attained, corresponding to flow Reynolds numbers $Re_f \sim 10^3$. This value is on the borderline for validity of the numerical calculations but is quickly reduced to $Re_f \sim 10^2$. As time proceeds the pressure waves are highly damped, buoyancy becomes the dominant mechanism and the Grashof number influences numerical stability. The computed values $Gr \sim 2 \times 10^4$ are well within the allowable range. To study further the resolution of the solutions, additional calculations were carried out for ten times the viscosity, thus decreasing Re_f by a factor of 10. Four cases were analysed: (i) $Re_f \sim 10^3$ for a 10×10 grid; (ii) $Re_f \sim 10^3$ for a 30×30 grid; (iii) $Re_f \sim 10^2$ for a 10×10 grid; (iv) $Re_f \sim 10^2$ for a 30×30 grid. The term resolution is defined herein as the percentage difference in the solution profiles

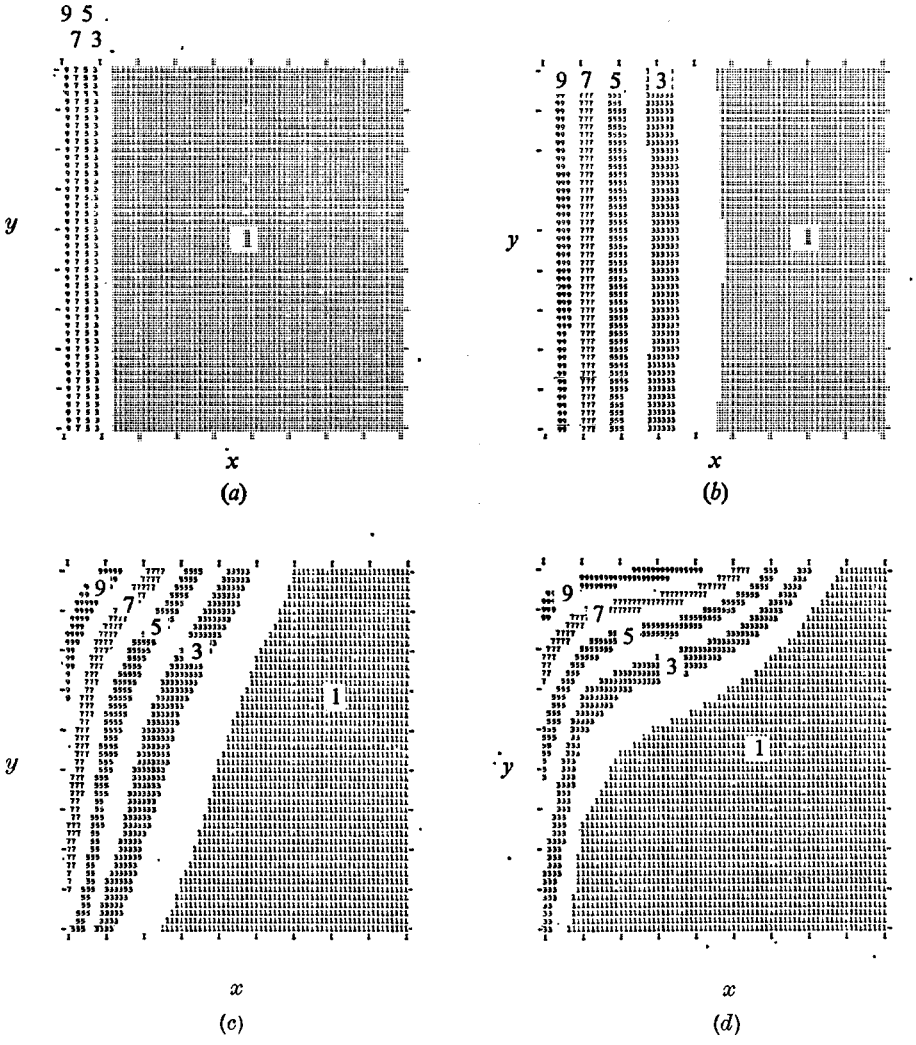

FIGURE 7. Temperature maps at $t = 20$ illustrating the effects of buoyancy- and pressure-driven convection. (10 = max, 1 = min.) (*a*) Conduction only: min = 1·0, max = 1·67. (*b*) $g = 0$: min = 1·0, max = 1·89. (*c*) $g = 0{\cdot}01$: min = 1·0, max = 1·92. (*d*) $g = 1{\cdot}0$: min = 1·0, max = 1·95.

obtained using two different grid sizes. A comparison of cases (i) and (ii) for all flow variables showed an average resolution of $\sim 6\,\%$. A comparison of cases (iii) and (iv) for all flow variables showed an average resolution of $\sim 4\,\%$. This indicates that the resolution becomes poorer as Re_f increases. The small relative difference between the comparisons lends further validity to use of the coarse grid for the cases $Re_f \sim 10^3$. Further, a comparison of cases (i) and (iii) indicates that numerical diffusion is not overshadowing real diffusion.

As time progresses, density gradients develop and give rise to buoyancy forces. Gravity-driven natural convection begins to cause circulation of the flow, which is now driven by both the pressure-gradient term and the body-force term in the

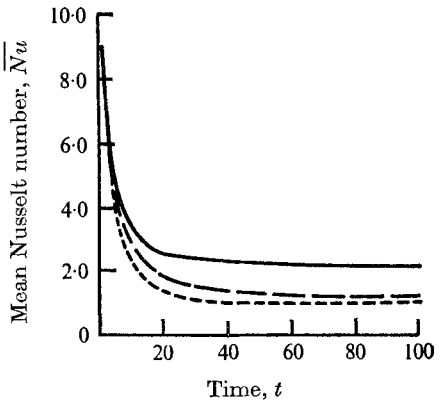

FIGURE 8. Mean Nusselt number *vs.* time. ——, $g = 1$; — —, $g = 0{\cdot}01$; – – – –, $g = 0$.

y-momentum equation. To investigate the relative strength of these driving mechanisms, four cases were run and maps of the isotherms were prepared at $t = 20$. These four cases, presented as figure 7, were the following: (*a*) conduction only; (*b*) convection for $g = 0$, i.e. pressure convection only; (*c*) combined convection for $g = 0{\cdot}01$; (*d*) combined convection for $g = 1{\cdot}0$.

Figure 7 (*a*) shows that the $T = 1$ isotherm still occupies about 85 % of the region for conduction only. Figure 7 (*b*) shows the effectiveness of pressure-driven convection in transferring heat from the wall $x = 0$. The $T = 1$ isotherm now occupies about 50 % of the region as heat is transferred from the wall through the fluid by the induced wave motion as well as by conduction. Figure 7 (*c*) shows the combined effect of buoyancy- and pressure-driven convection. We can analyse this effect by examining the position of the $T = 1$ isotherm. At the bottom of the region, the $T = 1$ isotherm is to the right of its position in the pure conduction case and to the left of that in the case $g = 0$. This shows that pressure-driven convection for $g = 0{\cdot}01$ is still effective in transferring heat in the x direction but is not as effective as in the $g = 0$ case. This is, of course, due to the buoyancy, which moves a portion of the hot fluid to the top of the region. Now note that the position of the $T = 1$ isotherm at the top of the region is to the right of that in figure 7 (*b*). The buoyancy-driven flow is thus transferring heat from the bottom of the container to the top by natural convection. Both driving mechanisms are thus influencing the unsteady temperature profile significantly for $g = 0{\cdot}01$.

Figure 7 (*d*) gives the temperature map for $g = 1$. Again a comparison of the $T = 1$ isotherm illustrates the relative strength of the driving forces. In figure 7 (*d*) we see that this isotherm is to the left of the one in figure 7 (*c*) at the bottom and to the right at the top of the region. In fact, the $T = 1$ isotherm at the bottom of figure 7 (*d*) is somewhat left of that shown in figure 7 (*a*) for pure conduction. At the top of the region, the $T = 1$ isotherm in figure 7 (*d*) is considerably to the right of that in any of the other cases. This is due to the dominance of buoyancy-driven convection for $g = 1$. For this configuration, fluid and boundary conditions, it is apparent that (i) pressure-driven convection is dominant in transferring heat at very low gravity, (ii) both pressure- and buoyancy-driven

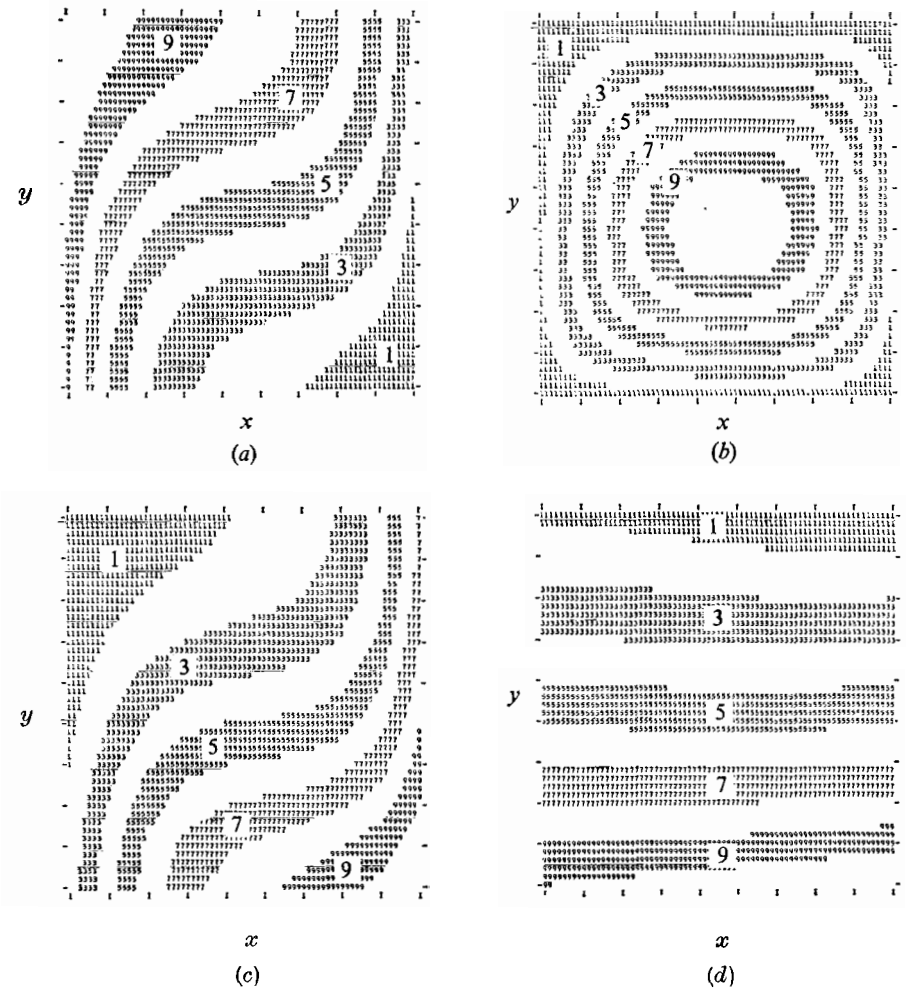

FIGURE 9. Steady-state contours for helium problem. (10 = max, 1 = min, $g = 1$.) (*a*) Temperature: min = 1·02, max = 1·97. (*b*) Stream function: min = $1{\cdot}1 \times 10^{-10}$, max = $5{\cdot}9 \times 10^{-5}$. (*c*) Density: min = 0·716, max = 1·42. (*d*) Total-pressure deviation from mean of 1·431: each band = 2×10^{-6}.

convection contribute significantly to the transient heat transfer at $g = 0{\cdot}01$, and (iii) buoyancy-driven convection is the dominant mechanism at $g = 1{\cdot}0$.

Figure 8 shows the mean Nusselt number as a function of time for the three cases. The mean value $\overline{Nu}$ was calculated by integrating the temperature gradient $\partial T/\partial x$ over all grid points at the left wall. The convergence to a steady state is indicated by the approach of $\overline{Nu}$ to a constant value. The steady-state value is $\overline{Nu} = 2{\cdot}12$ for $g = 1$, $\overline{Nu} = 1{\cdot}09$ for $g = 0{\cdot}01$ and $\overline{Nu} = 1{\cdot}0$ for $g = 0$. Figure 9 gives the steady profiles of the temperature, stream function, density and total pressure. The temperature and stream-function maps are similar in shape to the steady forms produced by numerical investigations of natural convection. The magnitudes appear to be very reasonable for the configuration, dimensionless

parameters and boundary conditions used. Density and total-pressure maps are not often seen in the literature on natural convection owing to the Boussinesq approximation. They are presented here to illustrate the total-solution profiles for a variable-density analysis. The density is seen to vary by a factor of approximately two between the minimum and maximum values. The mean pressure rise P_m in the container is calculated to be 1·431 in the steady state. The pressure gradients which exist in the steady state are shown in figure 9(*d*). These are mapped as contours of $P-P_m$ with each band representing a deviation of $2{\cdot}0 \times 10^{-6}$ from the mean value. The gradients are thus relatively small in magnitude in steady-state conditions but the contour map does show an interesting fact. The largest pressure gradients are in the vertical direction with much smaller gradients in the horizontal direction. The vertical gradients include both the static and dynamic components while the horizontal gradients consist of just a dynamic component. We can conclude, for this $g = 1$ case, that steady-state total-pressure gradients are small and that steady-state dynamic-pressure gradients do exist but are much smaller than the static component.

This work was supported in part by NASA-MSFC Contract NAS8-27015. The continuing interest and support of Mr T. C. Bannister, N.A.S.A. Contracting Officer's Representative, is gratefully acknowledged.

REFERENCES

Bannister, T. C. *et al.* 1973 *N.A.S.A. Tech. Memo.* X-64772.

Grodzka, P. G. & Bannister, T. C. 1972 *Science*, **176**, 506.

Harlow, F. H. & Amsden, A. A. 1971 *J. Comp. Phys.* **8**, 197.

Heinmiller, P. J. 1970 *T.R.W. Rep.* no. 17618-H080-R0-00. Houston, Texas.

Hellums, J. D. & Churchill, S. W. 1962 *A.I.Ch.E. J.* **8**, 690.

Knudsen, J. R. 1957 *J. Acoust. Soc. Am.* **26**, 51.

Larkin, B. K. 1967 *A.I.A.A. Paper*, no. 67-337.

Luikov, A. V. & Berkovsky, B. M. 1970 *Int. J. Heat Mass Transfer*, **13**, 741.

Richtmyer, R. D. & Morton, K. W. 1967 *Difference Methods for Initial Value Problems*, 2nd edn. Interscience.

Spradley, L. W. 1973 *12th Aerospace Sci. Meeting, A.I.A.A. Paper*, no. 74-76.

Spradley, L. W., Bourgeois, S. V., Fan, C. & Grodzka, P. G. 1973 *N.A.S.A. Contractor Rep.* no. 2269.

Thuraisamy, V. 1972 *Bellcom Rep.* TM-72-1022-1. Washington, D.C.

Torrance, K. E. 1968 *J. Res. Nat. Bur. Stand.* B **72**, 281.

Torrance, K. E., Davis, R., Eike, K., Gill, P., Gutman, D., Hsui, A., Lyons, S. & Zein, H. 1972 *J. Fluid Mech.* **51**, 221.

Trilling, L. 1955 *J. Acoust. Soc. Am.* **27**, 425.

Wilkes, J. O. & Churchill, S. W. 1966 *A.I.Ch.E. J.* **12**, 161.